Chapter 1

Seismic monitoring theory

1.1 Overview

In this chapter, I develop the mathematical relationships between fluid flow, rock physics and reflection seismology. The theory discussed here shows how to perform a complete run of the forward problem: simulate fluid flow, transform the fluid-flow results and a geologic description to saturated rock properties, and predict the resulting seismic reflection data. Similarly, I discuss the theory needed to perform the inverse problem: given seismic reflection data as input, make estimates of the short wavelength elastic impedance structure and long wavelength velocity structure, and infer fluid-flow properties in the subsurface from time-lapse seismic data sets. [1]

1.2 Introduction

Fluid flow plays many important roles in the Earth's crust, including: a resource of potable groundwater, a lubricant along earthquake fault surfaces, an exchange system with atmospheric fluids, and an association with natural energy resources such as geotherms, mineral deposits, and hydrocarbon reserves. To learn more about the role of fluids in crustal processes, remote sensing of fluid distribution and movement with time-lapse seismic monitoring data may prove to be an extremely useful technique. However, a good understanding of seismic time-lapse monitoring requires an integrated view of three traditionally separate disciplines: fluid flow, rock physics, and reflection seismology.

In this chapter, I link the physics of fluid-flow, rock mechanics, and seismic wave propagation, in the context of monitoring multi-phase flow in hydrocarbon reservoirs (?; ?). Figure 1.1 schematically shows how these three disciplines are coupled in the seismic fluid-flow monitoring problem, and how the critical physical parameters

[1] A modified version of this chapter was presented by Lumley (?; ?) at the Annual SPIE Conference, San Diego, CA, and received the Best Paper Award in the Mathematical Methods in Geophysical Imaging section.

in each discipline are related. The equations of fluid-flow describe changes in pore pressure p, temperature T, and multi-phase pore-fluid saturations S_i due to fluid flow in porous media. Rock physics transformations relate these fluid-flow parameters to seismic compressional-wave and shear-wave propagation velocities α and β. Elastic wave theory demonstrates that scattered wave amplitudes A and traveltimes τ of reflected seismic waves $\mathbf{u}^{PP}$ contain information about the fluid-flow parameters, and more importantly, that time-varying effects of fluid-flow may be decoupled from static background geology and imaged directly with time-lapse seismic data sets.

The first section deals with the theory of multi-phase fluid flow. Darcy's Law of fluid flow for simple porous media is coupled with a statement of fluid-flow mass balance. This leads leads to equations describing multi-phase flow in 3-D porous, permeable media. The next section deals with rock physics theory. The relationships between the bulk modulus K and shear modulus μ are given with respect to seismic compressional (P) and shear (S) velocities for dry porous rocks. Dry rock properties can be measured in the lab on core samples at varying confining pressure and temperature. Saturated rock properties are then given by Gassmann's equations as a function of the dry rock properties, pressure, temperature and fluid saturation. The last section describes how seismic wave propagation is related to fluid-flow and rock properties. This includes the equations to simulate seismic reflection data given an input earth model of saturated rock properties, and equations to image and estimate subsurface rock and fluid properties given an input seismic reflection data set.

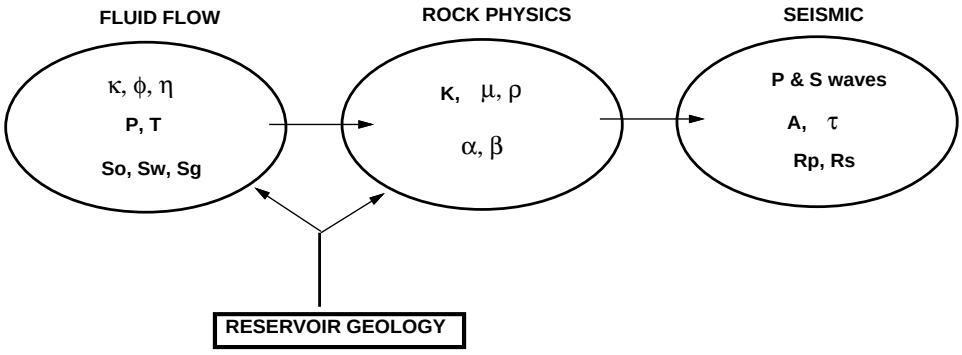

Figure 1.1: A schematic diagram showing the critical physical parameters in each discipline of fluid flow, rock physics, and seismic wave theory, and how they are naturally coupled together in the seismic fluid-flow monitoring problem. Fluid-flow parameters are permeability κ, porosity ϕ, viscosity η, pressure p, temperature T, and saturations S_i. Rock physics parameters are bulk and shear moduli K and μ, density ρ, compressional and shear velocities α and β. Seismic parameters are traveltime τ, amplitude A, compressional and shear reflectivities R_p and R_s. theory-forward [NR]

1.3 Fluid-flow theory

I consider a simple model of a hydrocarbon reservoir under production as an isothermal (constant reservoir temperature), immiscible (no chemical fluid mixing) three-phase fluid flow, as discussed for example by Dake (**?**). The three phases present in the pore space of the reservoir rock are oil, gas and water. During production, pore pressure decreases near oil producing wells, where fluids are withdrawn from the reservoir. Pore pressure increases near injection wells if gas or water is forced into the reservoir to maintain reservoir pressure during depletion, or to help drive oil towards the producing wells. The pressure variations cause three-phase fluid flow in the three spatial dimensions $\mathbf{x}$ of the reservoir as a function of production time t. This idealized model leads to the equations of 3-D multi-phase fluid flow by coupling the conservation of fluid-flow momentum and mass. More complex equations arise if the reservoir temperature is also variable, especially when extreme variations dynamically alter the viscosity and composition of the oil, as in a steamflood. Such complexity will not be addressed here.

1.3.1 Darcy's Law

Darcy's Law is an empirical relation which describes the observation that the rate of fluid-flow $q(x,t)$ across a surface of area A is proportional to the gradient of the fluid pressure $p(x,t)$,

$$q = -\frac{\kappa}{\eta} A \, \partial_x p \ , \tag{1.1}$$

for one-dimensional flow along the x-axis, as shown in Figure 1.2. A French civil engineer named Darcy (**?**) made observations of water flowing through sand packs. The flow rate was found to be directly proportional to the permeability $\kappa(x)$ of the porous medium, and when generalized to other fluid types, inversely proportional to the fluid viscosity $\eta(x)$, for a fixed pore pressure gradient.

Hubbert (**?**) showed that Darcy's Law is equivalent to the Navier-Stokes equation for conservation of fluid momentum. Darcy's Law is useful for geoscience applications because it describes the fluid flow in a macroscopic block of porous rock, which is representative of an upscaled average of the complex fluid flow at smaller scales (**?**).

1.3.2 Conservation of fluid-flow mass

The mass flux across the surface A per unit length is ρq, where $\rho(x)$ is the single-phase fluid density. The change in flux along the x-axis from x to $x + \Delta$ is therefore $\partial_x(\rho q)$. This flux change has to be balanced by the change in the fluid saturation S per unit length in the volume between x and $x + \Delta$, which can be written as $A\phi\partial_t(\rho S)$, and any amount of fluid injected per unit length into the volume, $\rho Q A$. ϕ is the rock

porosity, and Q is the injection fluid-flow rate per unit volume. These effects can be combined into a one-dimensional fluid-flow mass conservation equation:

$$\partial_x(\rho q) + A\phi\partial_t(\rho S) - \rho Q A = 0 \ . \tag{1.2}$$

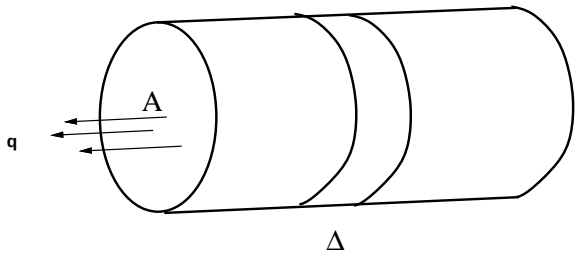

Figure 1.2: Darcy's Law is an empirical relation which describes the observation that the rate of fluid-flow $q(x,t)$ across a surface of area A is proportional to the gradient of the fluid pressure $p(x,t)$ for one-dimensional single-phase flow in porous media. theory-darcy [NR]

1.3.3 Multi-phase flow

Darcy's Law for the flow rate q can be substituted into the fluid-flow mass conservation equation (1.2), and extended to give a three-dimensional single-phase fluid-flow equation:

$$\nabla\left[\rho\left(\frac{\kappa}{\eta}\right)\nabla p\right] - \phi\partial_t(\rho S) = \rho Q \ . \tag{1.3}$$

This can further be extended to three separate fluid phases of oil, gas and water, yielding three coupled equations for 3-D multi-phase immiscible fluid flow (**?**),

$$\nabla\left(\frac{\kappa_o}{\eta_o}\nabla p_o\right) - \phi\partial_t S_o = Q_o \tag{1.4}$$

$$\nabla\left(\frac{\kappa_w}{\eta_w}\nabla p_w\right) - \phi\partial_t S_w = Q_w \tag{1.5}$$

$$\nabla\left[\rho_g\left(\frac{\kappa_g}{\eta_g}\right)\nabla p_g\right] - \phi\partial_t(\rho_g S_g) = \rho_g Q_g \quad . \tag{1.6}$$

The subscripts o, w, and g refer to oil, water and gas respectively. S_i is the saturation of the ith fluid component in the pore space on a scale from zero to unity, and Q_i is a fluid injection term which can represent fluid addition from an injection well (positive), or fluid withdrawal from a producing well (negative). p_i is the partial pressure for each phase of oil, gas or water. Equations (1.4) and (1.5) assume that oil and water are relatively incompressible fluids, whereas (1.6) captures the significant

expansion and compression effects of a gas under variable pressure conditions by including the gradient terms of gas fluid density ρ_g. These flow equations are coupled with the statements that the total pore saturation is complete and conserved with time:

$$S_w + S_o + S_g = 1 \tag{1.7}$$

$$\partial_t S_w + \partial_t S_o + \partial_t S_g = 0 \ . \tag{1.8}$$

Equations (1.4)–(1.8) are nonlinearly coupled and describe simple three-phase fluid flow in the hydrocarbon reservoir with production time. They are solved iteratively on a variable 3-D reservoir mesh by finite-difference or finite-element methods for the pressure and saturation spatial distributions at several time steps. An example of a fluid-flow simulation mesh is shown in Figure 1.3 for a faulted and uplifted reservoir in the Troll field, offshore Norway. The fluid-flow simulation of oil saturation after 113 days of depletion from a horizontal well is shown in Figure 1.4. This example will be discussed in detail in Chapter 3.

The important parameters to simulate are the evolution of the pore pressure and saturation changes in space and time. More complicated systems of equations are required to model complex thermal effects from steam injection processes, miscible floods in which the individual fluid phases are allowed to mix by chemical reaction, and other complicated phenomena such as oil fractionation, emulsions, fluid interfingering and gravity override.

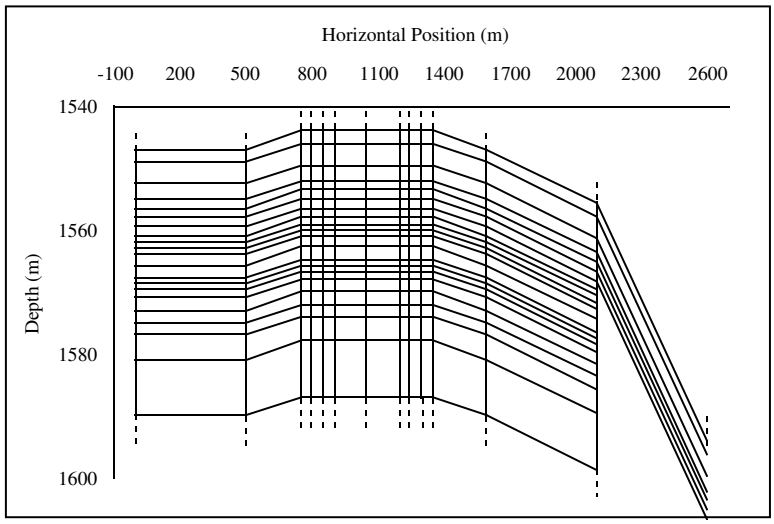

Figure 1.3: An expanded section of a reservoir fluid-flow simulation grid. theory-res-grid [NR]

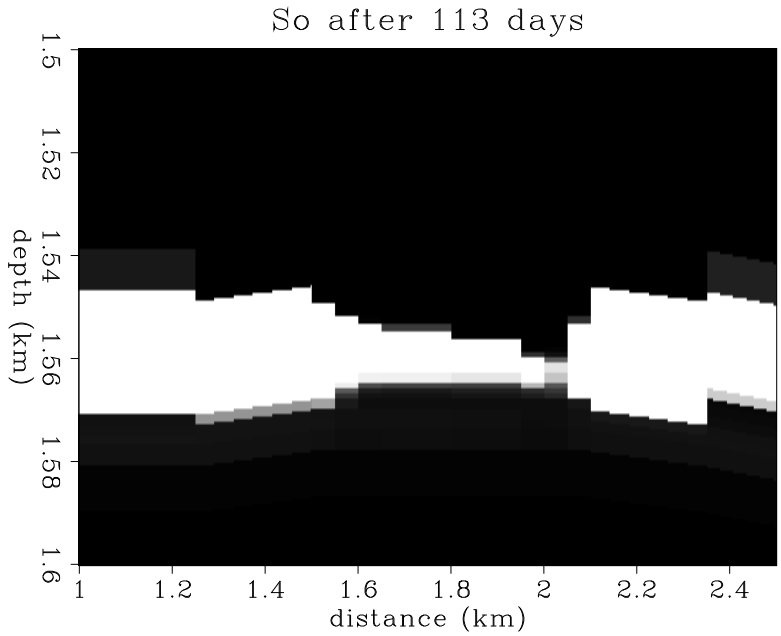

Figure 1.4: Simulated oil saturation distribution after 113 days of depletion from a horizontal well. 100% oil saturation is white, 0% saturation is black. theory-so3 [NR]

1.4 Rock physics transformations

Given the fluid-flow equations of the previous section, and some description of the reservoir geology, we can use rock physics analysis to transform reservoir pressure, temperature and fluid saturation data into seismic parameters. The most important parameters are the particle displacement velocities of the elastic waves that can propagate and scatter through the reservoir. These seismic wave velocities are denoted $\alpha(\mathbf{x})$ and $\beta(\mathbf{x})$ for the compressional (P) and shear (S) waves respectively.

Typically, dry rock properties for the reservoir are measured in the lab from core samples as a function of mineralogy, porosity, pressure and temperature. Then, effective fluid bulk moduli are computed for three-phase fluid mixtures of oil, gas and water, including the effects of temperature and pressure. Finally, saturated rock properties are calculated using Gassmann's equation by combining the dry-rock data and the effective fluid moduli as a function of pressure, temperature, porosity, and fluid saturation.

1.4.1 Dry rock properties

Rock cores obtained from boreholes in the reservoir are cleaned and oven-dried prior to dry rock measurements. Dry rock porosity ϕ and density ρ measurements are performed. Compressional and shear wave velocities are measured in the dry core samples with an ultrasonic wave generator, oscilloscope, and computer controlled measurement apparatus. Traveltimes for the P and S waves to propagate in the core

sample are measured at the 100 kHz to 1 MHz frequency range, and dry rock values for α and β are computed. Figure 1.5 shows an example of compressional waveforms measured across different core samples in a lab experiment, Lumley et al. (**?**). These measurements may be repeated under varying lab conditions of confining pressure and temperature to map out the response of a dry rock sample to reservoir pore pressure and temperature. Figure 1.6 shows an example of P- and S-wave velocities measured in dry Ottawa sandstone with varying pore pressure (**?**). Based on the dry α, β and ρ data, the dry bulk moduli K_{dry} and dry shear moduli μ_{dry} of the core samples can be obtained using the relation:

$$K_{dry} = \rho(\alpha^2 - \frac{4}{3}\beta^2) \quad ; \quad \mu_{dry} = \rho\beta^2 \,, \tag{1.9}$$

where ρ is the dry density.

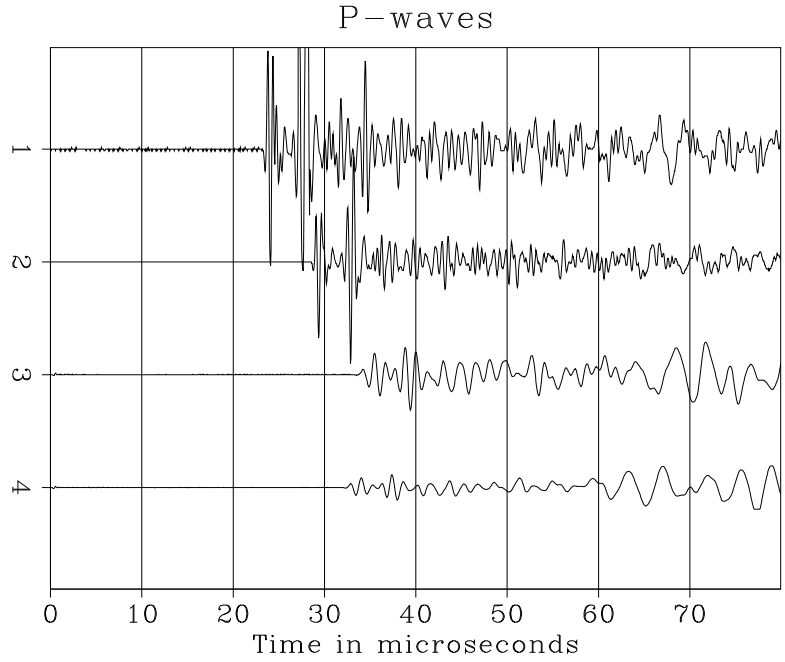

Figure 1.5: High-frequency compressional waveforms measured in various core samples under rock physics lab conditions. The lower two waveforms were measured in dry and saturated Massillon sandstone cores. theory-pwaves [NR]

Figure 1.6: Compressional and shear wave velocities in dry Ottawa sandstone versus pore pressure at 51 MPa overburden pressure (after Han, 1986). theory-vpvs-pp [ER]

1.4.2 Saturated rock properties

Unfortunately, ultrasonic lab measurements of saturated rock properties are not representative of field saturated rock properties in the surface-seismic frequency bandwidth

(10-200 Hz). This is due to dispersive wave effects caused by frequency-dependent fluid oscillations in the core sample pore space at ultrasonic frequencies. However, the velocity effect of saturation can be approximately estimated at surface seismic frequencies using Gassmann's quasi-static fluid substitution theory, e.g., Bourbié et al. (**?**). Gassmann's equation relates the elastic moduli of a dry rock to the elastic moduli of the same rock containing fluid at low frequencies:

$$K_{sat} = K_{solid}\,\frac{\phi K_{dry} - (1+\phi)K_{fluid}K_{dry}/K_{solid} + K_{fluid}}{(1-\phi)K_{fluid} + \phi K_{solid} - K_{fluid}K_{dry}/K_{solid}} \tag{1.10}$$

and

$$\mu_{sat} = \mu_{dry}\ , \tag{1.11}$$

where K_{sat} and μ_{sat} are the bulk and shear moduli of the saturated rock. Gassmann's relations require knowledge of the shear and bulk moduli of the dry rock (μ_{dry} and K_{dry}), the bulk modulus of the mineral material making up the rock (K_{solid}), the effective bulk modulus of the saturating pore fluid (K_{fluid}), and the porosity ϕ. Equation (1.10) is used to compute the low-frequency bulk modulus of saturated rock from high-frequency dry rock measurements. Equation (1.11) assumes that the shear modulus is independent of the amount of fluid saturation. Dry rock velocity measurements are assumed to be independent of the measurement frequency, which has been confirmed in the lab to first order.

For partially saturated rocks at sufficiently low frequencies, we can use an effective modulus K_{fluid} for an effective pore fluid that is an isostress average of the moduli of the liquid and gaseous phases:

$$\frac{1}{K_{fluid}} = \frac{S}{K_{liquid}} + \frac{(1-S)}{K_{gas}}\ . \tag{1.12}$$

This requires knowledge of the bulk modulus of the liquid phase (K_{liquid}), the bulk modulus of the gas phase (K_{gas}), and the saturation values (S). In general, if the pore fluid includes more than two phases, we can calculate the mixture's effective bulk modulus K_{fluid} based on the the number of fluid components N, the volumetric concentrations c_i of the ith component, and their bulk moduli K_i:

$$\frac{1}{K_{fluid}} = \sum_{i=1}^{N} \frac{c_i}{K_i}\ \ . \tag{1.13}$$

Combining equations (1.10) through (1.13), we can use the following formulas to estimate seismic velocities in saturated rocks:

$$\alpha_{sat} = \sqrt{\frac{(K_{sat} + \frac{4}{3}\mu_{sat})}{\rho_{sat}}} \tag{1.14}$$

and

$$\beta_{sat} = \sqrt{\frac{\mu_{sat}}{\rho_{sat}}} \, , \tag{1.15}$$

where ρ_{sat} is the density of the saturated rock:

$$\rho_{sat} = (1 - \phi)\rho_{solid} + \phi\rho_{fluid} \, , \tag{1.16}$$

ρ_{solid} is the density of the solid phase, and ρ_{fluid} is the density of the fluid mixture obtained as an arithmetic mean of the volume-weighted fluid density components ρ_i:

$$\rho_{fluid} = \sum_{i=1}^{N} c_i \rho_i \, . \tag{1.17}$$

This process allows us to calculate fluid properties that depend on fluid-flow saturation values. Figure 1.7 shows an example of dry rock measurements (labeled "gas") in Ottawa sandstone as a function of pore pressure, and the saturated velocities predicted by Gassmann's theory for 100% water, and 100% oil, saturated pore space (Jack Dvorkin, pers. comm.). The saturated properties will depend on pressure and temperature through the dry rock measurements, and through the variation in bulk modulus and density of reservoir gas. Pressure- and temperature-dependent gas properties may be calculated as discussed by Batzle and Wang (**?**). This total combined rock physics analysis allows us to calculate seismic velocities in saturated reservoir rock as a function of mineralogy, fluid type and saturation value, pore pressure and temperature. Therefore, we can map P-wave and S-wave velocity and density as a function of the reservoir grid directly from the fluid-flow simulation values of pressure, temperature, and oil, gas and water saturation.

Figure 1.7: Compressional velocity in Ottawa sand as a function of pore pressure and oil/water/gas saturation (Jack Dvorkin, SRB, pers. comm.). theory-vp-pp-sat [ER]

1.5 Seismic wave theory

Given the fluid-flow pressure, temperature and saturation data, mapped to seismic P-wave and S-wave velocity and density, the response of these fluid-flow changes can be modeled and imaged in seismic data by considering basic elastic wave theory.

1.5.1 Elastic wave modeling

Consider the elastodynamic wave equation for a seismic particle displacement vector wavefield $\mathbf{u}(\mathbf{x},\omega)$ and a second order tensor stress field $\boldsymbol{\sigma}(\mathbf{x},\omega)$ due to a body force vector excitation $\mathbf{f}(\mathbf{x},\omega)$:

$$\nabla\cdot\boldsymbol{\sigma} - \rho\omega^2\mathbf{u} = \mathbf{f} \ , \tag{1.18}$$

e.g., Aki and Richards (**?**). Assume further a linear elastic stress-strain relationship in the material continuum such that

$$\boldsymbol{\sigma} = \mathbf{C}{:}\nabla\mathbf{u} \ , \tag{1.19}$$

where $\mathbf{C}(\mathbf{x})$ is the fourth-order elastic stiffness tensor C_{ijkl}, and the ":" symbol means a second order inner contraction. A volume integral representation for the $\grave{P}\acute{P}$ "P-wave to P-wave" scattered wavefield $\mathbf{u}^{PP}$ can be expressed as:

$$\hat{\mathbf{a}}_r\cdot\mathbf{u}^{PP} = \int_{\mathcal{V}} \mathbf{f}^{P}\cdot\mathbf{u}^{P}\, d\mathcal{V} \ . \tag{1.20}$$

Equation (1.20) is the volume integral representation of the reflected $\grave{P}\acute{P}$ wavefield $\mathbf{u}^{PP}(\mathbf{x}_r,\omega;\mathbf{x}_s)$ measured at a receiver $\mathbf{x}_r$ along an arbitrary vector component direction $\hat{\mathbf{a}}_r$, due to the excitation of a body force reflection-diffraction scattering potential $\mathbf{f}^{P}(\mathbf{x};\mathbf{x}_s,\mathbf{x}_r)$ at each subsurface point $\mathbf{x}$, excited by the incident source wavefield $\mathbf{u}^{P}(\mathbf{x},\omega;\mathbf{x}_s)$ generated by a seismic source located at $\mathbf{x}_s$.

The assumption of isotropic elastic WKBJ (ray-valid) Green's tensors for P waves leads to:

$$\mathbf{u}^{P}(\mathbf{x},\omega;\mathbf{x}') = A^{P}(\mathbf{x};\mathbf{x}')\ \hat{\mathbf{t}}^{P}(\mathbf{x};\mathbf{x}')\ e^{i\omega\tau(\mathbf{x};\mathbf{x}')} = A^{P}\hat{\mathbf{t}}^{P}e^{i\omega\tau} \ , \tag{1.21}$$

where A^{P} and τ are the ray-valid P-wave amplitude and traveltime from the "source" location $\mathbf{x}'$ to the "observation" point $\mathbf{x}$, and are related by the eikonal and transport equations respectively (**?**):

$$|\nabla\tau|^2 = \nabla\tau\cdot\nabla\tau = \frac{1}{\alpha^2} \tag{1.22}$$

$$A\ \nabla^2\tau + 2\nabla\tau\cdot\nabla A = 0 \ . \tag{1.23}$$

The unit vector $\hat{\mathbf{t}}^{P}$ is the direction parallel to P-wave propagation, as shown in Figure 1.8, and is perpendicular to the wavefronts $\tau = \text{constant}$.

For a linear isotropic elastic solid, the stress-strain relationship is

$$\boldsymbol{\sigma}^{P} = \left[\lambda(\nabla\cdot\mathbf{u}^{P})\mathbf{I} + 2\mu\nabla\mathbf{u}^{P}\right] = \frac{i\omega}{\alpha}\left[\lambda(\hat{\mathbf{t}}^{P}\cdot\mathbf{u}^{P})\mathbf{I} + 2\mu\hat{\mathbf{t}}^{P}\mathbf{u}^{P}\right] \ , \tag{1.24}$$

where $\lambda(\mathbf{x})$ and $\mu(\mathbf{x})$ are the Lamé parameters such that

$$\lambda = \rho\alpha^2 \quad \text{and} \quad \mu = \rho\beta^2 \ , \tag{1.25}$$

and $\mathbf{I}$ is the second-order identity matrix δ_{ij}. Lumley and Beydoun (**?**) have shown that a representation of the P-wave reflection-diffraction scattering potential $\mathbf{f}^{P}$ is:

$$\mathbf{f}^{P} = -\frac{i\omega}{\alpha^2}|\mathbf{u}^{P}|\left[(\alpha\nabla\lambda - \lambda\nabla\alpha) + 2(\alpha\nabla\mu - \mu\nabla\alpha)\cdot(\hat{\mathbf{t}}^{P}\hat{\mathbf{t}}^{P})\right] \ . \tag{1.26}$$

Equation (1.26) is a *body force equivalent* for scattering-surface reflectivity excitations, and is dependent upon the material property contrasts (gradients): $\nabla\alpha$, $\nabla\lambda$ and $\nabla\mu$.

After some algebraic manipulation, (1.20) can be represented as:

$$\hat{\mathbf{a}}_r\cdot\mathbf{u}^{PP}(\mathbf{x}_r) = \int_{\mathcal{V}} \rho\omega^2 \cos a_r A_s A_r e^{i\omega\tau_{sr}} \grave{P}\acute{P} \cos\phi_r \, d\mathcal{V}(\mathbf{x}) \ . \tag{1.27}$$

To interpret (1.27), the density at a subsurface point $\mathbf{x}$ is denoted $\rho(\mathbf{x})$, and the geometric reflection coefficient at that point is $\grave{P}\acute{P}(\mathbf{x})$. The amplitude terms A_s and A_r represent the cumulative geometric spreading, transmission loss, Q-attenuation, etc., from the source and receiver to the subsurface point $\mathbf{x}$ respectively. The factor $\cos a_r$ involves the vector component projection at the surface location $\mathbf{x}_r$ of $\mathbf{u}^{PP}$ onto the arbitrary direction $\hat{\mathbf{a}}_r$. The term $\tau_{sr} = \tau_s + \tau_r$ is the total traveltime from the source at $\mathbf{x}_s$ to the subsurface point $\mathbf{x}$ and back up to the receiver at $\mathbf{x}_r$. Finally, the diffraction weight $\cos\phi_r$ represents the angle between the anticipated geometric specular reflection direction $\hat{\mathbf{t}}_s^{PP}$ and the non-geometric diffraction direction $\hat{\mathbf{t}}_r^{P}$. In the case of specular reflection when $\hat{\mathbf{t}}_s^{PP} = \hat{\mathbf{t}}_r^{P}$, $\phi_r = 0$ and so $\cos\phi_r = 1$. The generalized reflection ray and angle geometries are shown in Figure 1.8.

A linearized version of the nonlinear $\grave{P}\acute{P}$ reflection coefficient can be parameterized in terms of impedances as:

$$\grave{P}\acute{P}(\mathbf{x}, \cos\bar{\theta}) \approx 0.5\sec^2\bar{\theta}\,\frac{\Delta(\rho\alpha)}{(\rho\alpha)} - 4\gamma^2\sin^2\bar{\theta}\,\frac{\Delta(\rho\beta)}{(\rho\beta)} + \left(2\gamma^2\sin^2\bar{\theta} - 0.5\tan^2\bar{\theta}\right)\frac{\Delta\rho}{\rho} \ , \tag{1.28}$$

where $\gamma = \beta/\alpha$ and $\bar{\theta}$ is the reflection angle between the incident wave direction $\hat{\mathbf{t}}^{P}$ and the local gradient of the compressional P-impedance structure $\nabla(\rho\alpha)$. To first order in $\bar{\theta}$, the $\grave{P}\acute{P}$ reflectivity is proportional to relative P-impedance contrasts $\Delta(\rho\alpha)/(\rho\alpha)$.

The contributions from shear impedance and density contrasts are second and third order respectively.

An equivalent linearization is given in a velocity parameterization by Aki and Richards (**?**), but is less robust for the purposes of inverting seismic reflection data because velocity and density cannot be unambiguously decoupled at small $\bar{\theta}$. For forward modeling, either linearization is accurate when the relative perturbations in impedance and density are small, and the reflection angles $\bar{\theta}$ are less than the critical angle at which conical "head waves" emerge.

The seismic modeling equations (1.22), (1.23), (1.27) and (1.28) show that changes in fluid-flow pressure, temperature and saturation, mapped to α, β and ρ changes through rock physics transformations, will have an effect on the traveltimes τ and reflection amplitudes $\grave{P}\acute{P}$ in the seismic data $\mathbf{u}^{PP}$. If several seismic surveys are recorded at different phases of production fluid-flow, the seismic response will change with calendar time due to the coupled equations in fluid-flow, rock physics and elastic wave theory shown above. For example, Figure 1.9 shows modeled CMP gather seismograms, after moveout correction, before and after oil production from a horizontal well. This example will be discussed in more detail in Chapter 3. The next section addresses the topic of imaging changes in fluid-flow directly from multiple seismic data sets recorded in "monitoring" mode.

Figure 1.8: Generalized reflection ray and angle geometries. theory-anglegeom [ER]

1.5.2 Seismic wavefield imaging

Given a seismic data set recorded at some calendar time T_1, we would like to be able to image the subsurface reflectivity structure R_1 which generated the reflected waves observed in that seismic data. Furthermore, we would like to obtain several reflectivity estimates $R_1, R_2, R_3, ...$ corresponding to surveys over a producing reservoir at calendar times $T_1, T_2, T_3...$, and infer something about the change in subsurface fluid flow from the changes in the R_i maps. The required imaging procedure is called "seismic migration" in the seismic exploration industry (**?**).

I briefly derive a "kinematic" Kirchhoff prestack depth migration equation which is suitable for either 2-D or 3-D data acquisition, and incorporates single-arrival traveltime and phase estimates. This migration equation yields accurate estimates of reflectivity amplitudes for near-offset data, and provides an efficient and robust structural imaging condition for all offset data, as shown by Lumley (**?**).

Given the Helmholtz variable-velocity α scalar wave equation

$$\left\{\nabla^2 + (\omega/\alpha)^2\right\} P(\mathbf{x},\omega) = S(\mathbf{x},\omega)\ , \tag{1.29}$$

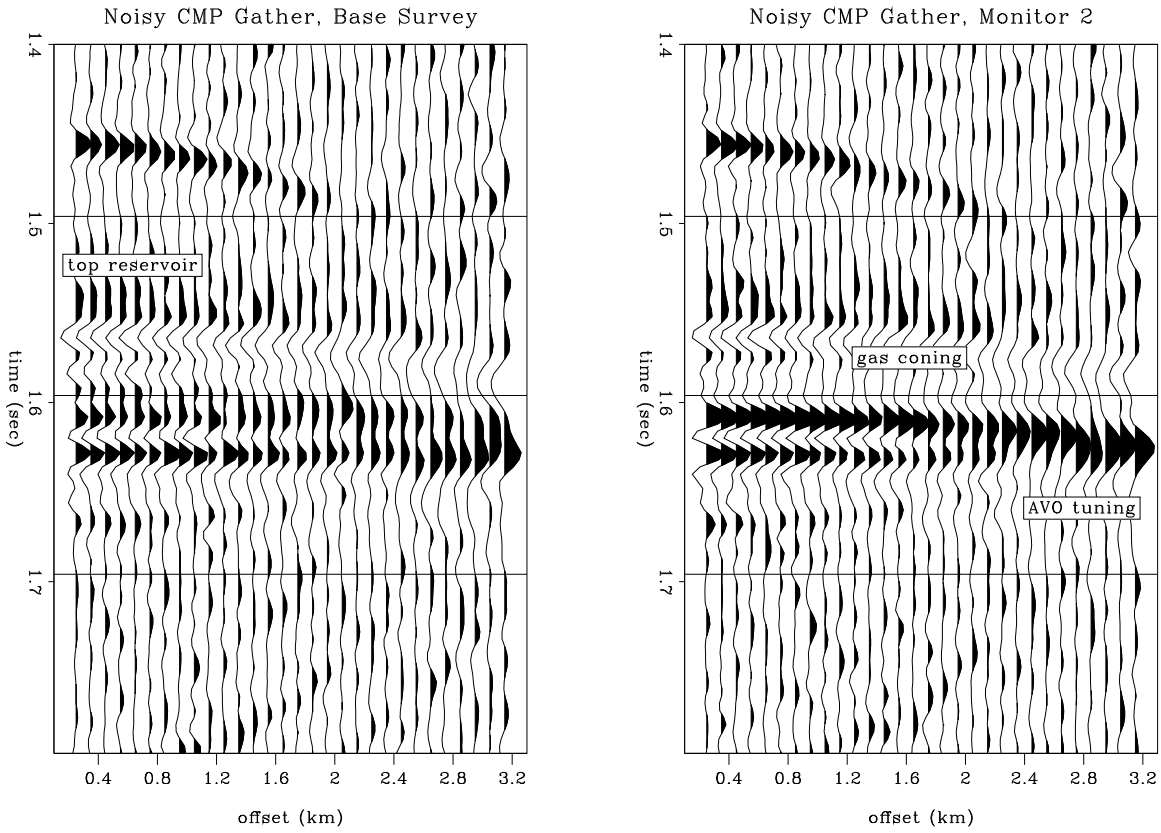

Figure 1.9: Modeled CMP gather seismograms, before and after oil production from a horizontal well. Note near offset waveform traveltime and amplitude changes, and far offset AVO tuning. theory-noise13-ann [NR]

the "downgoing wavefield" D generated by a single source at location $\mathbf{x}_s$ can be evaluated at any subsurface location $\mathbf{x}$ within a volume $\mathcal{V}$ from the frequency-domain integral representation:

$$D(\mathbf{x},\omega;\mathbf{x}_s) = \int_{\mathcal{V}} G(\mathbf{x},\omega;\mathbf{x}')\ S(\mathbf{x}',\omega;\mathbf{x}_s)\ d\mathbf{x}'\ , \tag{1.30}$$

where $G(\mathbf{x},\omega;\mathbf{x}')$ is the Green's function solution to (1.29) associated with the source location, and S is the source wave function. If we neglect the absolute amplitude of the source and consider only relative amplitudes in the migrated section, and assume the source has a compact delta function shape in both space and time: $\delta(t)\delta(\mathbf{x}'-\mathbf{x}_s)$, then the downgoing wavefield can be approximated by the source Green's function alone: $D(\mathbf{x},\omega;\mathbf{x}_s) \approx G(\mathbf{x},\omega;\mathbf{x}_s)$.

The "upgoing wavefield" U reflected from the subsurface $\mathbf{x}$ due to a source at $\mathbf{x}_s$ can be reconstructed from the seismic (scalar) data $P = \hat{\mathbf{a}}_r \cdot \mathbf{u}^{PP}$ recorded at receivers $\mathbf{x}_r$ using a Kirchhoff integral representation:

$$U(\mathbf{x},\omega;\mathbf{x}_s) = \int_{\mathcal{S}} \hat{\mathbf{n}}\cdot\nabla G(\mathbf{x},\omega;\mathbf{x}_r)\ P(\mathbf{x}_r,\omega;\mathbf{x}_s)\ d\mathbf{x}_r\ , \tag{1.31}$$

where $G(\mathbf{x},\omega;\mathbf{x}_r)$ is the receiver Green's function and $\hat{\mathbf{n}}$ is the unit vector normal to the recording surface $\mathcal{S}$ that bounds the image volume $\mathcal{V}$ of interest. The gradient operator ∇ is taken with respect to the subsurface coordinate $\mathbf{x}$ along the recording surface at $\mathbf{x} = \mathbf{x}_r$.

Given that the reflected wavefield U can be modeled as a convolution of the subsurface reflectivity R with the source wavefield D, a local least-squares estimate of R can be obtained as the weighted zero-lag correlation of the source and reflected wavefields: $R \approx \sum_\omega W\ U\ D^*$, where W are as yet unspecified weights, and D^* is the complex conjugate of D. If this weighted zero-lag correlation is further averaged for all such single shot-profile migrations, the frequency-domain Kirchhoff migration equation becomes:

$$R(\mathbf{x}) \approx \int_\omega \int_{\mathbf{x}_s} \int_{\mathbf{x}_r} W\ [\hat{\mathbf{n}}\cdot\nabla G(\mathbf{x},\omega;\mathbf{x}_r)]\ G^*(\mathbf{x},\omega;\mathbf{x}_s)\ P(\mathbf{x}_r,\omega;\mathbf{x}_s)\ d\mathbf{x}_r\ d\mathbf{x}_s\ d\omega\ . \tag{1.32}$$

It can be shown that the reflectivity image R is proportional to a reflection-angle averaged version of the $\grave{P}\acute{P}$ coefficient in the modeling equation (1.27), and is a first order estimate of the relative P-wave impedance contrast in the earth, as inferred from equation (1.28):

$$R\ \approx <\grave{P}\acute{P}> \approx\ \frac{\Delta(\rho\alpha)}{(\rho\alpha)} + O(\sin^2\bar{\theta})\ . \tag{1.33}$$

I next assume a parametric form for the Green's functions G such that:

$$G(\mathbf{x},\omega;\mathbf{x}_a) \approx A_a(\mathbf{x};\mathbf{x}_a)\; e^{\pm i(\omega\tau_a+\phi_a)}\;, \tag{1.34}$$

where opposite signs are chosen in the exponential for the source (outgoing) and receiver (reverse-time extrapolated) Green's functions respectively. The parameters A_a, τ_a and ϕ_a are the single-arrival Green's function amplitudes, traveltimes and phase rotations from location $\mathbf{x}_a$ to $\mathbf{x}$. These parameters are often estimated by conventional high-frequency asymptotic ray methods.

Given the parametric form (1.34), an efficient time-domain version of (1.32) can be obtained as:

$$R(\mathbf{x}) \approx \int_{\mathbf{x}_s}\int_{\mathbf{x}_r} \cos\theta_r\; \hat{W}\; e^{i\phi_{sr}}\hat{P}(\mathbf{x}_r,\mathbf{x}_s;t=\tau_{sr})\; d\mathbf{x}_r\, d\mathbf{x}_s\;, \tag{1.35}$$

where the "obliquity factor" $\cos\theta_r$ is a function of the incident angle at each receiver with respect to the surface normal, and is obtained as the dot product $(\alpha_r\nabla\tau_r\cdot\hat{\mathbf{n}})$. The Kirchhoff space-time migration equation (1.35) is a weighted diffraction stack of the preprocessed, deconvolved (but not divergence-corrected) data $\hat{P}$, after phase-rotation by the Green's function parameters $\phi_{sr} = \phi_s + \phi_r$, evaluated along the diffraction trajectories given by the Green's function traveltimes $\tau_{sr} = \tau_s + \tau_r$.

I define *kinematic* migration by setting the migration weights $\hat{W}$ to unity. I note that (1.35) is suitable for 2-D migration if all spatial coordinates are 2-vectors, e.g. $\mathbf{x} = (x,z)$, and $\hat{P}$ is preprocessed by the half-time derivative operator $\sqrt{i\omega}$. However, (1.35) is equally suitable for 3-D migration if all spatial coordinates are 3-vectors, e.g. $\mathbf{x} = (x,y,z)$, and $\hat{P}$ is preprocessed by the full time derivative ∂_t.

1.5.3 Seismic velocity analysis

The seismic migration equation (1.35) images subsurface reflectivity structure, which is proportional to short-wavelength impedance variation. However, (1.35) is a non-linear function of wave propagation velocity α to first order in traveltimes τ, and to second order in amplitudes A. The coherency of any reflectivity image is therefore dependent upon the accuracy to which the long-wavelength velocity structure α is known. Velocity estimation is nonlinear, and reflectivity estimation is linear, given a smooth estimate of the background velocity field. In general, the problem of estimating the short-wavelength reflectivity and the long-wavelength velocity are nonlinearly coupled, and need to be solved simultaneously. In practice, the problem is usually assumed to be separable and solved sequentially: first for the velocity and next for the reflectivity.

A general nonlinear inverse problem can be posed to solve for long-wavelength velocity and short-wavelength impedance as follows. A measure of coherency can be defined as some function $\mathcal{F}$ of the reflectivity image R, which is itself a function of the velocity α,

$$\text{Coherency} \quad = \quad \mathcal{F}\{R(\alpha)\} \; . \tag{1.36}$$

Since the image is assumed to be most coherent at the correct velocity model, a nonlinear optimization problem ensues, e.g., Symes and Carazzone (?). An optimal velocity solution is obtained when the coherency does not improve with slight adjustments to the velocity model:

$$\frac{\partial \mathcal{F}\{R(\alpha)\}}{\partial \alpha} \quad = \quad 0 \quad \rightarrow \quad \alpha(\mathbf{x}) \; . \tag{1.37}$$

Equation (1.37) is the gradient of the image coherency with respect to velocity perturbation, and can be used in a nonlinear steepest-descent or conjugate-gradient method to iterate towards a final solution.

1.5.4 Seismic fluid-flow monitoring

The seismic migration equation (1.35) can be used to obtain an estimate of the subsurface reflectivity R for any seismic data set. This reflectivity image is an estimate of the elastic $\grave{P}\acute{P}$ scattering coefficient averaged over all reflection angles, and is, to first order, proportional to the short-wavelength P-wave impedance contrasts, $R_p = \Delta(\rho\alpha)/(\rho\alpha)$, in the subsurface. If equation (1.35) is re-expressed as a common-offset migration, "image gathers" can be constructed to estimate the angle-dependent reflectivity at each point in the subsurface (?; ?). In this case the entire $\grave{P}\acute{P}$ linearization (1.28) can be fit to the image gather in an "AVO analysis" (?) to estimate both P-impedance and S-impedance relative contrasts R_p and R_s at each subsurface point (?; ?; ?).

Information on the long-wavelength velocity structure $\alpha(\mathbf{x})$ is available in the seismic data from the traveltime information τ_{sr} in the wavefield $\mathbf{u}^{PP}$, by solution of the nonlinear velocity analysis system (1.37). The velocity structure α and reflectivity image of R (or R_p and R_s) estimated from a single seismic survey will be comprised of coupled contributions from the reservoir geology and the fluid-flow states in pore space. The estimation and interpretation of this information from a single seismic data set can be defined as *seismic reservoir characterization*:

$$\text{Characterization} \quad = \quad \alpha(\mathbf{x}),\; R_p(\mathbf{x}),\; R_s(\mathbf{x}) \quad \rightarrow \quad \text{rock + fluid} \; .$$

Seismic reservoir characterization is a very difficult task because of the ambiguity in trying to decouple geology effects from fluid-flow effects in a single seismic data set.

However, when multiple seismic surveys are conducted at separate calendar times, it is expected that the reservoir geology will not change from survey to survey, but the state of fluid flow will change. Therefore, differencing a series of reflectivity images R_i and velocity model estimates α_i will remove the static geologic contribution to the seismic data, and isolate time-varying seismic changes in the reservoir which are due

to time-varying fluid-flow changes alone. The process of estimating and comparing reflectivity images and velocity estimates from multiple seismic data sets recorded at different calendar times can be defined as *seismic reservoir monitoring*,

$$\text{Monitoring} \;=\; \partial_t \;\{\, \alpha(\mathbf{x},t),\; R_p(\mathbf{x},t),\; R_s(\mathbf{x},t) \,\} \;\rightarrow\; \text{fluid flow}\,.$$

Seismic reservoir monitoring is potentially a much less ambiguous task than characterization, because the effects of geology and fluid-flow may be decoupled by comparing time-varying seismic data sets.

Figure 1.10 shows a dramatic example of the changes observed in a seismic monitor data set recorded over a steam injection site. The left panel is a migrated reflectivity section before steam injection, the center panel is a migrated reflectivity section after 5 months of steam injection, and the third panel is the difference between the two seismic results. Note the changes visible in the third panel due to a shallow borehole steam leak (B), the steam injection zone (S), and a possible transient pressure front (P). This data set will be discussed in more detail in Chapters 4 and 5.

1.6 Conclusion

I have discussed the physical theory relevant for three-phase fluid flow in a producing oil reservoir, and rock physics transformations of fluid-flow pressure, temperature and pore-fluid saturation values to seismic P-wave and S-wave velocity. I have linked fluid-flow physical parameters to seismic reflection data amplitudes and traveltimes through elastic wave-equation modeling and imaging theory. I have shown examples of both synthetic and field data which demonstrate that changes in fluid-flow can be monitored and imaged under certain conditions from repeated seismic surveys acquired at varying production calendar times.

1.7 Acknowledgments

I thank Amos Nur, Gary Mavko, Jack Dvorkin, and Jim Berryman for their many helpful discussions of rock physics.

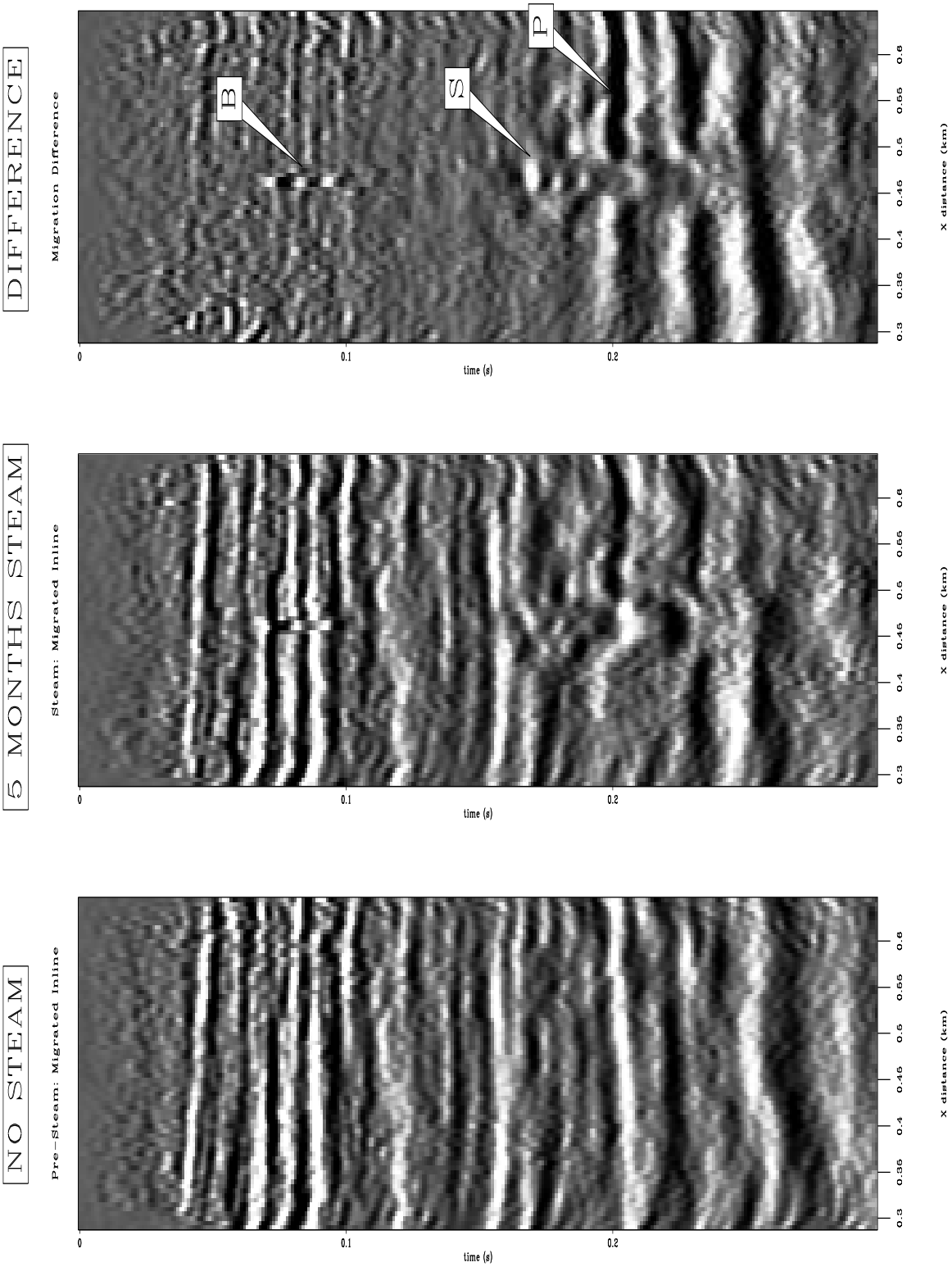

Figure 1.10: 3-D migrated seismic time-lapse sections: before steam injection (left), during steam (center), and the difference (right). "S" marks the steam zone, "B" marks borehole heating by a possible steam leak, and "P" marks a polarity reversal possibly caused by a transient pressure front. theory-inline-migs-ann [NR]